Euler Solutions for Aircraft Configurations Employing Upper-Surface Blowing

Essam Atta,* Saad Ragab,† and Larry Birckelbaw,‡
Lockheed Georgia Company, Marietta, Georgia

A zonal method has been developed for computing the flowfield around aircraft configurations using upper-surface blowing. The method is based on a zonal grid generation approach coupled with an Euler flow solver algorithm. In this method the flowfield is divided into a number of nonoverlapped regions, each containing a component of the aircraft such as a wing, a fuselage, or a nacelle. H-type grids are generated independently in each region using a hybrid elliptic/algebraic grid generation scheme. An explicit finite-volume Euler algorithm has been developed that is applicable to the multiregion H-type grids. The present method has been applied to a three-dimensional upper-surface blowing model and a realistic aircraft configuration consisting of a wing/fuselage with two integrated nacelles. Numerical results indicate that the computational method is effective in predicting the flowfield about upper-surface blowing-type configurations and complex aircraft geometries.

Introduction

RECENT advances in developing numerical algorithms for solving fluid flow problems and the continuing improvement in the speed and storage of large-scale computers have made it feasible to compute the flowfields for a variety of aircraft configurations. However, because of the increasing complexities of both the geometries and flowfields encountered in practical aircraft aerodynamic simulation, accurate prediction of the flowfield is difficult to achieve. For example, the high-speed engine/airframe integration problems of systems such as upper-surface blowing (USB) and over-the-wing blowing (OTW) configurations are particularly difficult as a result of the engine placement and the interaction of the propulsion flowfield with the configuration surfaces.

Although grid generation methods have been developed to a high degree of sophistication (Refs. 1-4), difficulties in constructing computational finite-difference grids often arise because of the geometric complexities of multicomponent aircraft configurations. Grid generation for such configurations is best treated using zonal grid generation methods. The basic idea of these methods is to develop separate grid systems for the individual components of a complex configuration; the component grids are then joined along common boundaries (Refs. 5 and 6) or allowed to overlap (Refs. 7-10) to form the finite-difference grid for the complete configuration.

In the present paper, a method is developed to compute the flowfield about complex multicomponent aircraft configurations that use the upper-surface blowing concept. The flowfield is computed using the Euler formulation so that strong shock waves are treated accurately and flow rotationality is resolved properly. The grid generation method employs a zonal patched grid approach that allows a high degree of adaptability to a variety of complex aircraft configurations. The following sections describe the implementation of the method for wing/fuselage/nacelle configurations.

Received May 19, 1985; presented as Paper 86-1767 at the AIAA 4th Applied Aerodynamic Conference, San Diego, CA, June 9-12, 1986; revision received Nov. 7, 1986.

*Scientist, Advanced Flight Sciences Department. Member AIAA.
†Assistant Professor, Engineering Science and Mechanics Department, Virginia Polytechnic Institute and State University. Member AIAA.
‡Associate Scientist, Advanced Flight Sciences Department.

Grid Generation

The present zonal grid generation method is based on a hybrid differential/algebraic scheme and an H-type grid topology. The grid for a multicomponent configuration such as a wing/fuselage/nacelle combination is constructed by generating a global grid for the wing and local grids for the fuselage and the two nacelles. The component grids are smoothly patched together along common surfaces. This approach simplifies the communication of the flow information between the different components and permits greater control of grid-point distribution, skewness, and clustering.

Wing Component Grid

The global grid (wing grid) is generated by solving a set of two-dimensional elliptic partial differential equations for a series of span stations that define the wing surface. These equations are solved using a standard SLOR algorithm. Source terms in the elliptic equations are computed from the wing surface grid point distribution (Ref. 11). Off the wing tip, the grid is generated for wing sections of zero thickness. Taper, sweep, and twist variations are accounted for by using a sequence of coordinate rotations. Clustering of the spanwise stations in the vicinity of the wing root, tip, and span location of the nacelle is achieved by using fourth-order polynomials. Near the wing leading and trailing edges, exponential stretching is used to control grid spacing.

Fuselage and Nacelle Component Grids

The fuselage and nacelle grids are generated using cubic polynomials for a series of two-dimensional planes along the fuselage and nacelle axes. The nacelle inlet is closed by a dome-shaped cap. The aft portion of the nacelle is extended downstream as a solid plume surface. When exhaust jet effects or inlet flow need to be considered, separate internal grids are generated and matched with the nacelle grid. Exponential stretching formulas[12] are used to control the grid point distribution, and Bezier curves[13] are used to smoothly patch the fuselage and nacelle grids with the wing grid.

The effectiveness of the grid generation method in representing complex aircraft configurations is illustrated in Figs. 1-7, which show different views of the surface and field grids for a typical wing/fuselage/nacelle configuration. These figures illustrate the smooth transition of grid lines from the fuselage to the wing/nacelle region. Regions of high surface curvature and lines of component intersection are modeled properly as shown in Fig. 5. A nacelle can be treated as either a

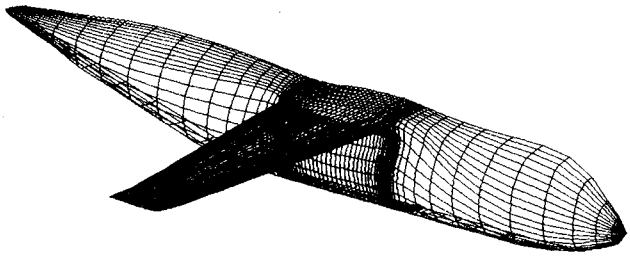

Fig. 1 Surface grid for a high-wing/fuselage configuration.

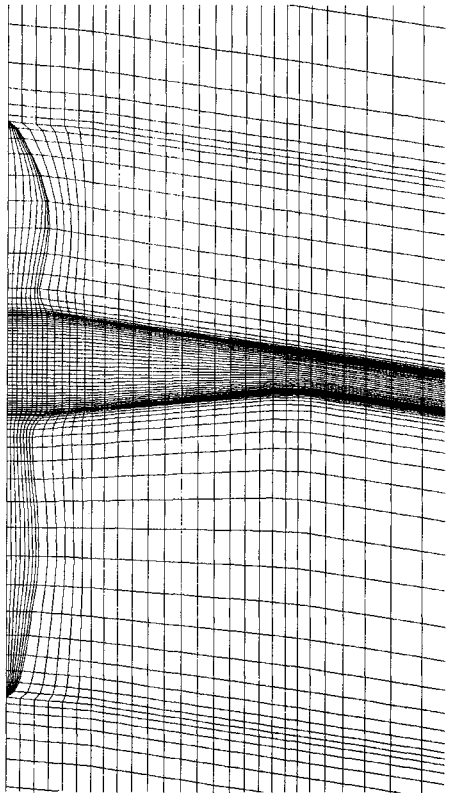

Fig. 2 Top view of the field grid for a wing/fuselage configuration.

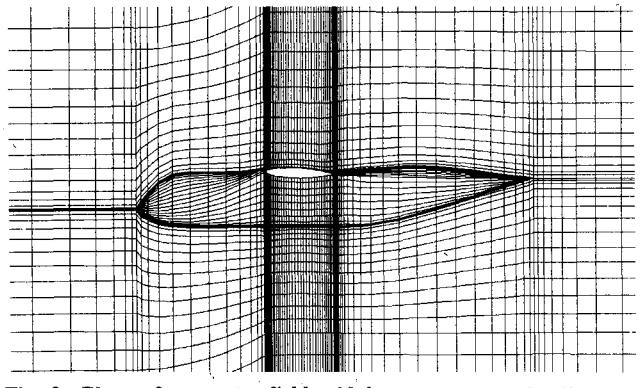

Fig. 3 Plane of symmetry field grid for a transport wing/fuselage configuration.

solid external store, a nacelle with a closed inlet, or a complete nacelle including both inlet and exhaust regions. The initial surface grids for the various nacelle components are shown in Figs. 6 and 7.

The grid generation scheme has been implemented into a modular package that provides a high degree of adaptability for complicated geometries. The zonal structure of the gridding scheme combined with the use of the H-type topology allows the grid generation scheme to be used for isolated components or complex configurations. Computations were performed on the CRAY XMP-24 and a medium grid of about 200,000 grid points for a wing/fuselage with two nacelles requires about 20 s of CPU time.

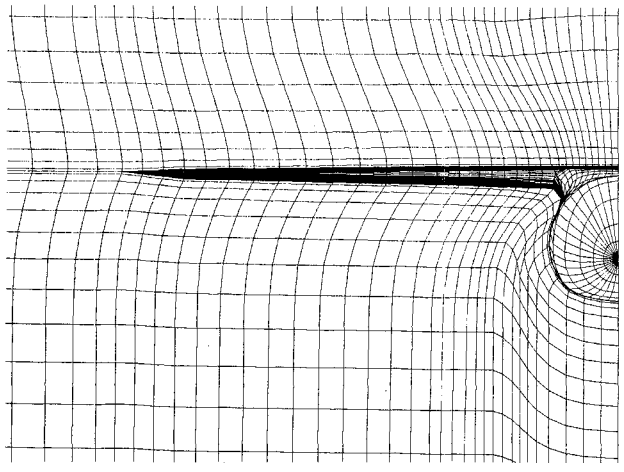

Fig. 4 Front view of the field grid for a wing/fuselage configuration.

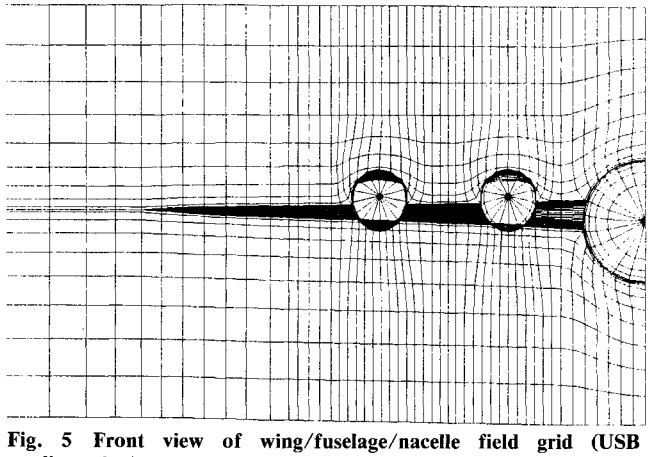

Fig. 5 Front view of wing/fuselage/nacelle field grid (USB configuration).

Flow Solver

The Euler flow solver algorithm is based on the finite-volume time-stepping Runge-Kutta scheme of Ref. 14. Details of the numerical algorithm can be found in Refs. 14 and 15. In the present method, the flow solver has been structured to operate within the framework of the zonal H-grid topology and to allow the analysis of single or multicomponent configuration. The flowfield solution is obtained by sequential sweeping through each component grid. For a single component, the flow variables are updated to an intermediate time level before advancing to the next stage in the Runge-Kutta scheme, whereas for a multicomponent configuration, the flow variables are updated to the new time level block by block.

To reduce computer storage requirements, the number of three-dimensional arrays is kept to a minimum. Only the flowfield solution variables and the grid coordinate arrays are stored for all blocks; other arrays are recomputed before starting the solution for a given block. In this way, arrays containing information such as cell volumes, local time steps, and the artificial dissipation associated with only a single block are present at any time. This arrangement allows a larger number of grid blocks to be considered without the use of special input/output devices.

Because of the central differencing employed in the Euler flow solver, artificial viscosity has to be added to the numerical algorithm. The explicit addition of artificial viscos-

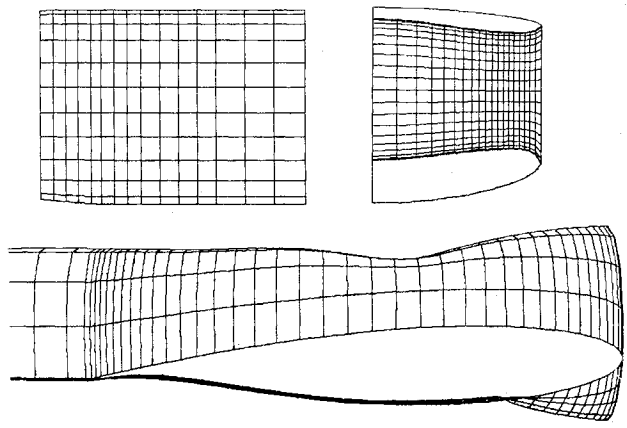

Fig. 6 Initial surface grids for the nacelle components.

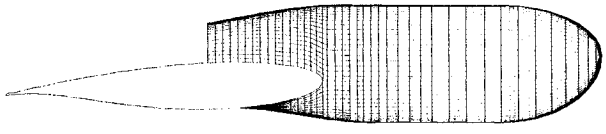

Fig. 7 Side view of the surface grid for USB wing/nacelle with closed inlet.

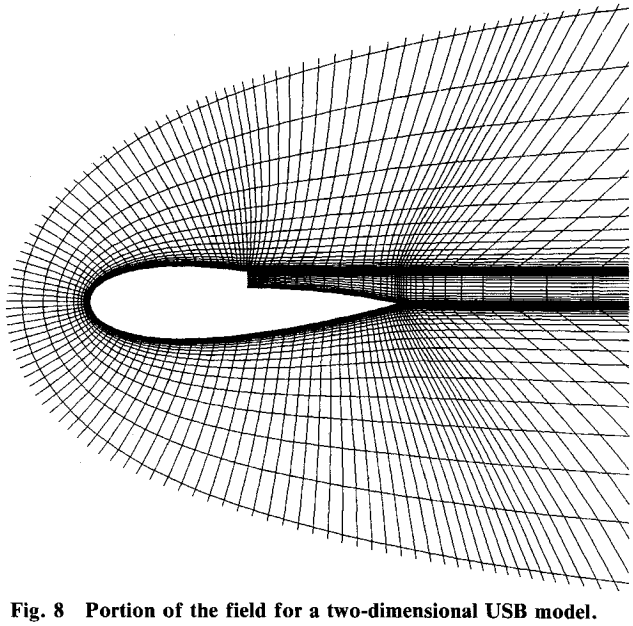

Fig. 8 Portion of the field for a two-dimensional USB model.

ity involves dissipation constants that have to be adjusted for each problem, and thus can lead to a less robust numerical algorithm. However, the flexibility of tailoring the artificial viscosity for each individual problem and the coding simplicity of central differencing schemes can be very beneficial. The problem of introducing artificial viscosity into central differencing numerical schemes can be eliminated by using upwind differencing,[16] which will provide a built-in artificial viscosity. Nevertheless, in cases where no viscosity is needed, it is difficult to turn it off, since the viscosity is built into the differencing scheme. Further, upwind differencing involves complex logic and requires more computational work, especially if used within the multiblock structure of the present flow solver.

Appropriate boundary conditions are imposed on all computational boundaries. Solid surfaces boundary conditions are accomplished by setting all the convective fluxes to zero. Far-field boundary conditions are specified depending on whether inflow, outflow, subsonic, or supersonic flow conditions exist.

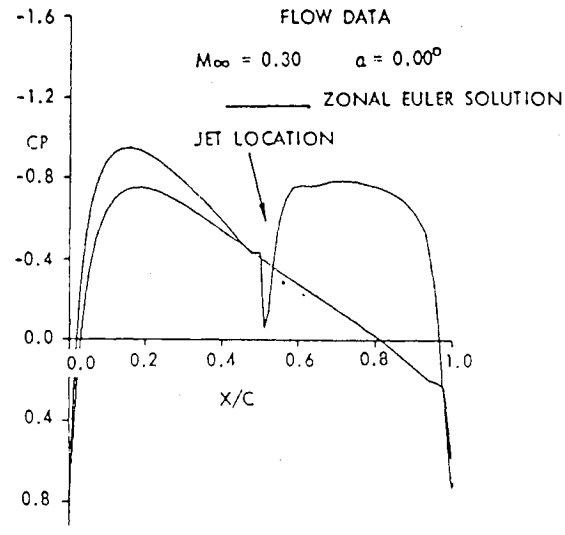

Fig. 9 Surface pressure distribution for two-dimensional USB model (jet pressure ratio = 1.6).

For subsonic exhaust jets, the ratio of the jet total pressure to freestream static pressure and jet inclination angle are specified, while the jet exit static pressure is extrapolated. For supersonic jets, the jet total pressure ratio, jet Mach number, and jet inclination angle are specified. In either case, the total enthalpy is assumed constant. At the zonal boundaries between adjacent blocks, flow continuity is imposed. Thus, the boundary conditions for a given block are established using interior grid points from the adjacent block.

Because the H-grid topology is used in each of the different zones, and a one-to-one correspondence of grid points between the zonal boundaries is maintained, proper flux conservation across the zonal boundaries does not require a special treatment such as the one reported in Ref. 17. The only error that might occur will be caused by the grid skewness and stretching near the zonal boundaries, and that can be controlled by properly adjusting the grid lines across the zonal boundaries.

Computational Results

Two-Dimensional USB Model

To investigate the effectiveness of the Euler formulation in modeling exhaust jet flows and to evaluate the performance of the numerical algorithm in conjunction with the multiblock grid strategy, numerical experiments were carried out on a two-dimensional USB model representing a wing/nacelle cross section. Figure 8 shows the model and the associated grid. The grid was constructed using two blocks, an inner block for the exhaust plume region and an outer block for the remainder of the flowfield.

Figures 9 and 10 show the computed pressure distributions obtained on the configuration of Fig. 8 for two exhaust pressure ratios. The high suction peaks that the jet action induced on the model surface were predicted by the computational model. Furthermore, the sensitivity of the computational procedure to variations in the exhaust pressure ratio is clearly evident. Figure 11 displays computed velocity vector plots at a distance of 10 to 12 chords in the far field downstream of the wing/nacelle combination. The figure shows that the general character of the flow in the exhaust plume region is captured, and the expected downward deflection of the jet is displayed in the computed results.

Numerical experimentation performed on the two-dimensional model indicated that the sequential block-by-block updating of the flow variables did not significantly impair the algorithm convergence rate. However, to maintain smooth and continuous flow variations, the artificial damping coefficients used in the Euler solver to stabilize the numerical

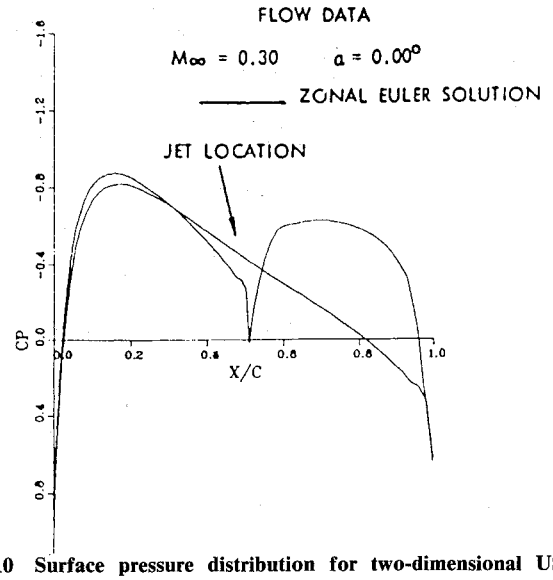

Fig. 10 Surface pressure distribution for two-dimensional USB model (jet pressure ratio = 1.6).

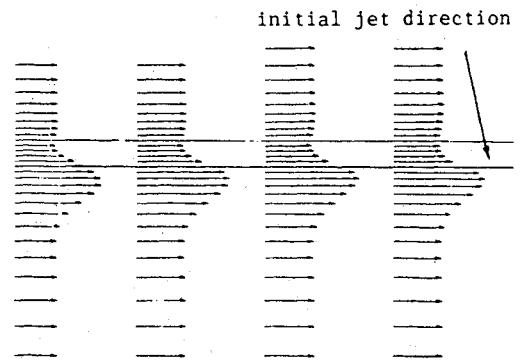

Fig. 11 Computed jet velocity profiles in the downstream far field of the two-dimensional wing/nacelle model (jet pressure ratio = 1.6).

algorithm had to vary for each block, with higher values used in the jet exhaust region. Typical values for the fourth- and second-order dissipation coefficients are (0.05, 0.01) for the outer block and (0.01, 1.0) for the jet block. The variation of these coefficients did not affect the solution convergence, but it was necessary to smooth out oscillations in the flowfield solution near the exhaust jet exit and the trailing edge region.

Three-Dimensional Configurations

Computed results are compared with the experimental data of Ref. 18. These experiments were conducted in the NASA Lewis 8×6 ft tunnel for a representative four-engine short-haul aircraft employing upper-surface blowing. The test model consisted of a fuselage of circular cross section, a supercritical wing, and two nacelles. Both symmetric and streamlined nacelles were employed in the experimental investigation. A top view of the test configuration is shown in Fig. 12.

Correlation of the computed Euler results and test data was performed for wing/fuselage and wing/fuselage with two nacelles at a freestream Mach number of 0.7. Shown in Fig. 13 are comparisons of the computed wing surface pressure distribution, the experimental data, and the panel method results of Ref. 16. The Euler solutions are in better agreement with the experimental data as compared to the panel method results. The high suction peak near the wing leading edge is captured and generally good agreement is achieved, except on

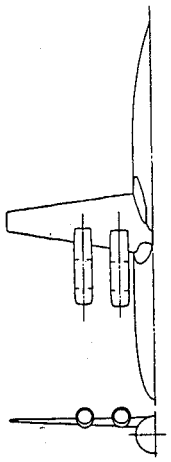

Fig. 12 Test model for a short-haul aircraft employing upper-surface blowing.

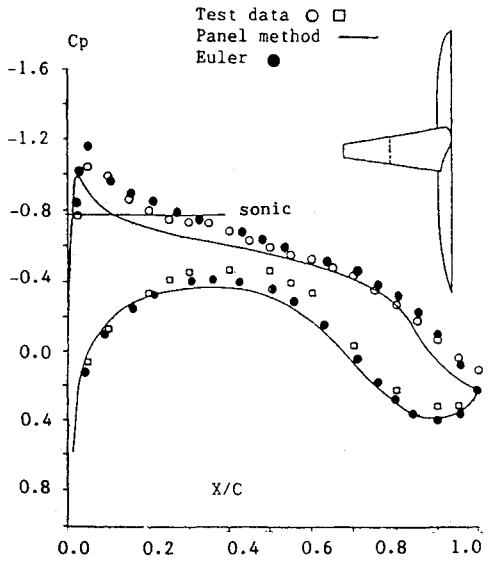

Fig. 13 Comparison of computed and experimental pressure distribution (freestream Mach number = 0.7, angle of attack = 0.5 deg).

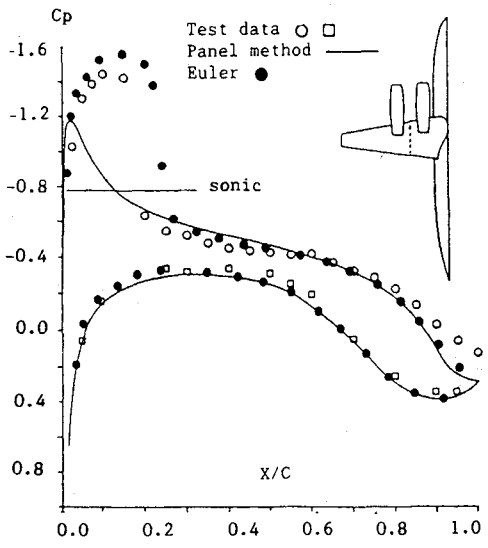

Fig. 14 Comparison of computed and experimental pressure distribution (freestream Mach number = 0.7, angle of attack = 0.5 deg).

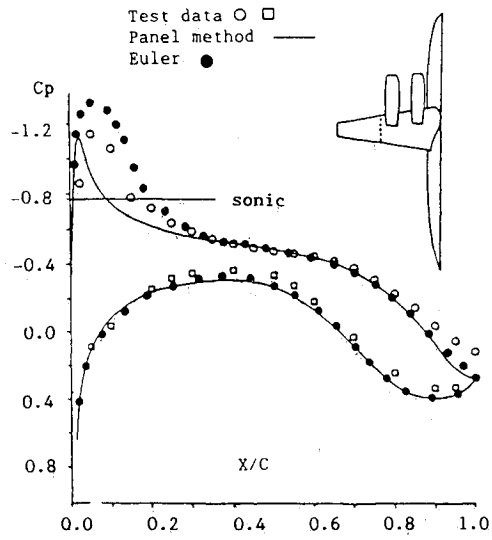

Fig. 15 Comparison of computed and experimental pressure distribution (freestream Mach number = 0.7, angle of attack = 0.5 deg).

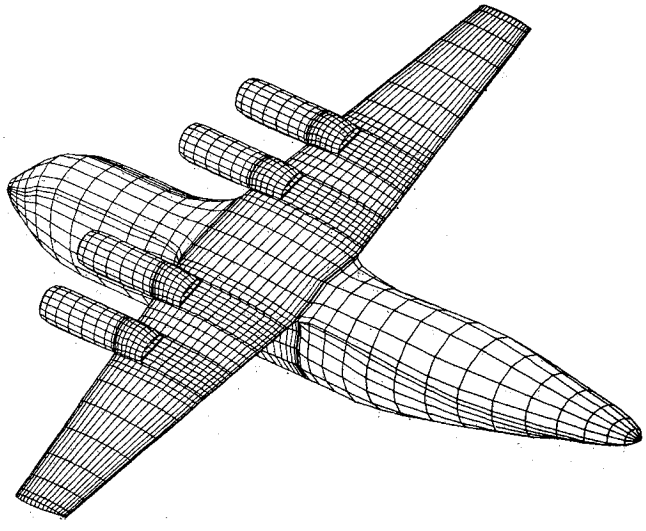

Fig. 16 High-lift transport cruise configuration model.

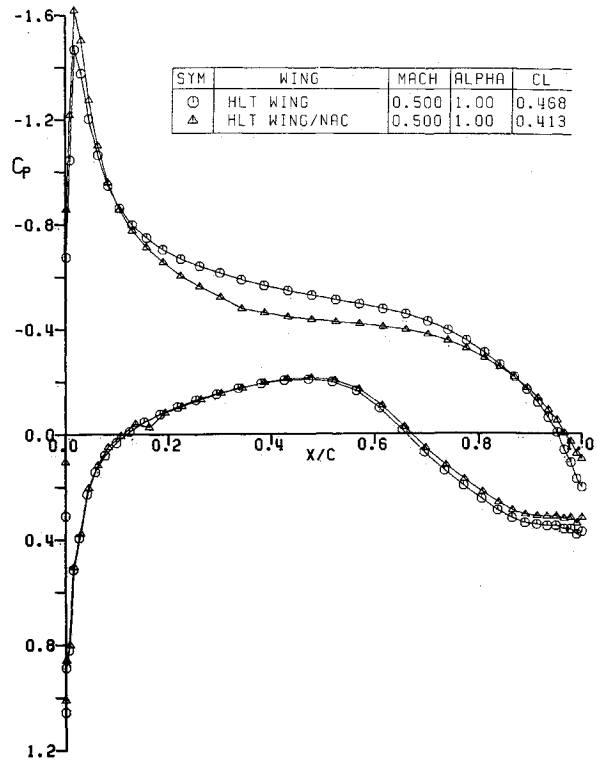

Fig. 17 Nacelle effect on wing pressure distribution (inboard station at 25% span, Nacelle centerline at 35% span, freestream Mach number = 0.5, angle of attack = 1.0 deg).

the lower surface near the wing trailing edge region that is dominated by viscous effects.

Correlations of the computed and measured wing surface pressure distributions for the test model with the two nacelles installed are shown in Figs. 14 and 15. Good agreement is obtained for the outboard wing station shown in Fig. 14, although the suction level on the wing upper surface near the leading edge is overpredicted. The correlation for the inboard station shown in Fig. 15 is less satisfactory with regard to shock location and strength. The Euler solution produced a stronger shock, and furthermore, the computed shock location is about 10% chord aft of the experimentally observed one. As expected, the panel method results compared very poorly with the test data.

To identify the nacelles' interference effects at different flow conditions, another set of computations was performed for the Lockheed designed wing/fuselage/nacelle configuration of Fig. 16. The computations were performed for freestream Mach numbers of 0.5 and 0.75 at an angle of incidence of 1.0 deg. Figures 17-20 present surface pressure distributions for two span stations inboard and outboard of the nacelle. As shown in Figs. 17-20, the nacelle interference has a significant effect on the wing upper surface pressure distribution, especially near the wing leading edge and at high speeds. The nacelle interference effect combined with the wing sweep has distorted the flowfield structure in such a way that negative pressures develop on the wing inboard side and positive pressures on the outboard side; at high speeds, the nacelle blockage effect has caused a pronounced forward movement of the shock on the wing upper surface.

To validate the computed Euler results for USB configurations with jet effects, correlations have been performed with the upper-surface blowing experimental data of Ref. 19. The test configuration consists of a USB wing/nacelle combination typical of a USB commercial transport. The details of the experimental setup are documented in Ref. 20. Correlations are made for a Mach number of 0.6, angle of attack of 2.0 deg, and a jet total pressure ratio of 1.8. Figure 21 shows a pressure comparison between the computed Euler results, the vortex lattice method of Ref. 20, and experimental data. The experimental pressure data are measured on the wing surface aft of the nacelle jet exit, and are expressed as increments above the clean-wing conditions. The computed Euler results are in good agreement with the experimental data. The high suction peak caused by the jet toward the wing trailing edge has been reproduced. Furthermore, good correlation is obtained near the jet exit region. The vortex lattice results of Ref. 20 overpredict the pressure levels and correlate well with the experimental data only near the wing trailing edge.

All the computations were performed on the CRAY XMP-24 computer using a computational grid of 200,000 points that correspond to 3.3 million words of the CRAY central memory. The grid consisted of 82 streamwise stations, 49 spanwise stations, and 50 normal stations. Because of computer storage constraints, the computations were performed for either a wing/fuselage, a wing/two nacelles, or wing/nacelle with jet effects. In a typical computed solution, the residual is reduced by three orders of magnitude in 700 steps, and this requires about one hour of CPU time on the CRAY XMP-24.

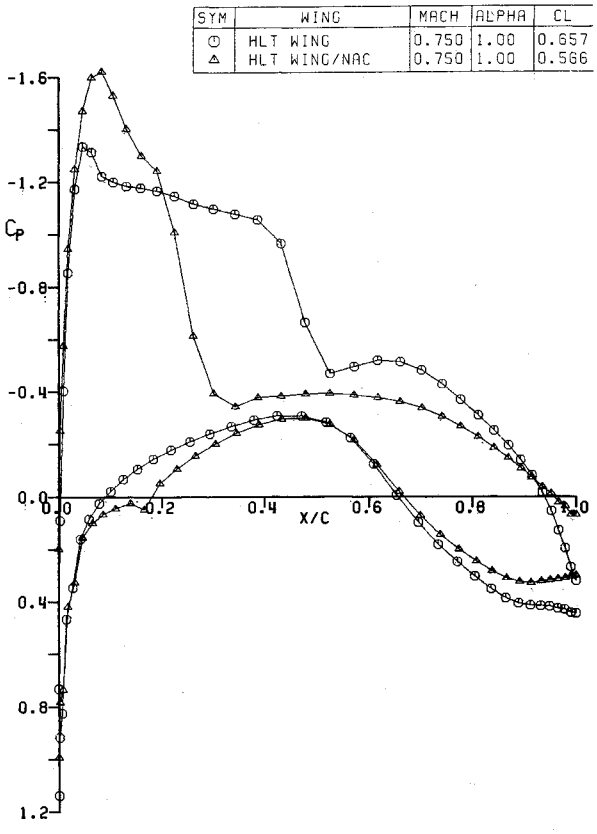

Fig. 18 Nacelle effect on wing pressure distribution (inboard station at 28% span, Nacelle centerline at 35% span, freestream Mach number = 0.75, angle of attack = 1.0 deg).

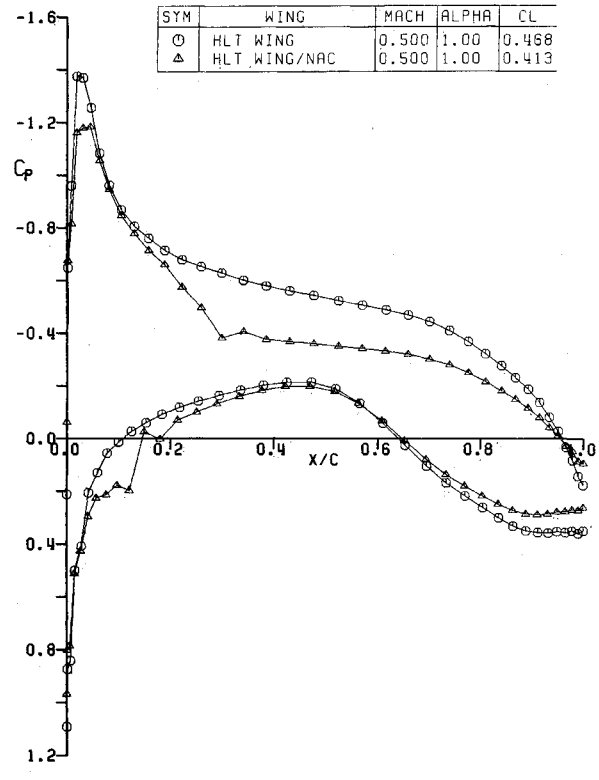

Fig. 19 Nacelle effect on wing pressure distribution (outboard station at 47% span, Nacelle centerline at 35% span, freestream Mach number = 0.5, angle of attack = 1.0 deg).

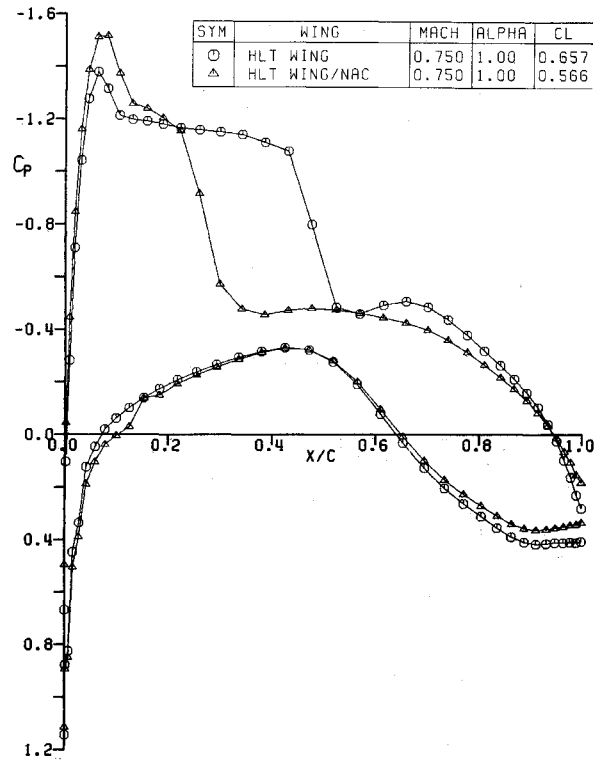

Fig. 20 Nacelle effect on wing pressure distribution (outboard station at 50% span, Nacelle centerline at 35% span, freestream Mach number = 0.75, angle of attack = 1.0 deg).

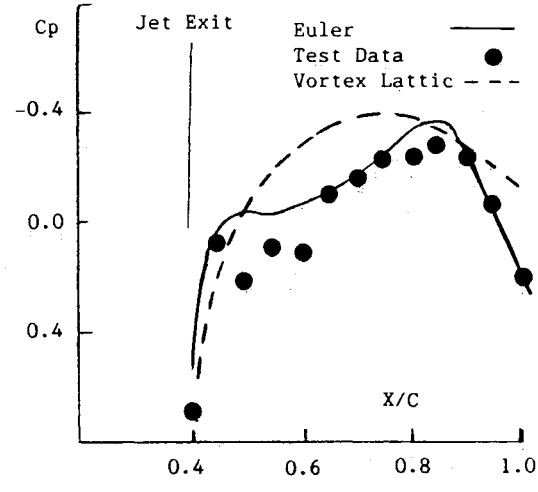

Fig. 21 Comparison of computed and experimental pressure distribution in the exhaust jet region of a USB wing/nacelle configuration.

Conclusions

A zonal grid generation method has been developed and coupled with an Euler flow solver to compute the flowfield about aircraft configurations employing upper-surface blowing. The use of the H-type grid topology and the finite-volume flow solver proved to be very effective for treating multicomponent configurations. The correlation of the computed flowfield solutions with experimental data demonstrates the ability of the present method to capture the essential features of complex flowfields. Future development of the method will provide a useful engineering tool for the aerodynamic analysis of practical aircraft configurations.

References

[1]Thompson, J.F., "Grid Generation Techniques in Computational Fluid Dynamics," *AIAA Journal*, Vol. 22, Nov. 1984.

[2]Thompson, J.F., "Numerical Grid Generation," edited by J.F. Thompson, North-Holland, New York, 1982.

[3]Thompson, J.F., "A Survey of Composite Grid Generation Methods for General Three-Dimensional Regions," *Proceedings of the International Meeting on Advances in Nuclear Engineering Computational Methods*, Vol. 1, Knoxville, TN, April 1985.

[4]Atta, E.H., "Zonal Methods and Computational Fluid Dynamics," *Proceedings of the International Meeting on Advances in Nuclear Engineering Computational Methods*, Vol. 1, Knoxville, TN, April 1985.

[5]Weatherill, N.P. and Forsey, C.R., "Grid Generation and Flow Calculations for Complex Aircraft Geometries Using a Multiple Block Scheme," AIAA Paper 84-1665, 1984.

[6]Yu, N.J., Samant, S.S., and Rubbert, P.E., "Flow Prediction for Propfan Configurations Using Euler Equations," AIAA Paper 84-1645, 1984.

[7]Atta, E.H. and Vadyak, J., "A Grid Overlapping Scheme For Flowfield Computations About Multicomponent Configurations," *AIAA Journal*, Vol. 21, Sept. 1983.

[8]Atta, E.H., "Component-Adaptive Grid Interfacing," AIAA Paper 81-0382, Jan. 1981.

[9]Benek, J.A., Steger, J.L., and Dougherty, F.C., "A Flexible Grid Embedding Technique With Application to the Euler Equations," AIAA Paper 83-1944, 1983.

[10]Benek, J.A., Buning, P.G., and Steger, J.L., "A 3-D Chimera Grid Embedding Technique," AIAA Paper 85-1523, July 1985.

[11]Thomas, P.D. and Middelcoff, J.F., "Direct Control of the Grid Point Distribution in Meshes Generated by Elliptic Equations," *AIAA Journal*, Vol. 18, June 1980.

[12]Vinokur, M., "On One-Dimensional Stretching Functions for Finite-Difference Calculations," NASA CR 3313, 1980.

[13]Rogers, D.F. and Adams, J.A., *Mathematical Elements for Computer Graphics*, McGraw-Hill, New York, 1976.

[14]Jameson, A., Schmidt, W., and Turkel, E., "Numerical Solutions of the Euler Equations by Finite Volume Methods Using Runge-Kutta Time-Stepping Schemes," AIAA Paper 82-1017, 1982.

[15]Jameson, A. and Baker, T.J., "Solution of the Euler Equations for Complex Configurations," AIAA Paper 83-1929, July 1983.

[16]Thomas, J.L. and Walters, R.W., "Upwind Relaxation Algorithms for the Navier Stokes Equations," AIAA Paper 85-1501, July 1985.

[17]Raj, M.M., "A Conservative Treatment of Zonal Boundaries for Euler Calculations," AIAA Paper 84-0164, Jan. 1984.

[18]Wells, O.D., "Wind Tunnel and Analytical Investigation of Over-The-Wing Propulsion/Air Frame Interferences for a Short-Haul Aircraft at Mach Numbers from 0.6 to 0.78," NASA CR-2905, 1977.

[19]Braden, J.A., Hancock, J.P., Hackett, J.E., Burdges, K.P., and Lyman, V., "Exploratory Studies of the Cruise Performance of Upper Surface Blown Configurations," NASA CR-3192, June 1980.

[20]Braden, J.A., Hancock, J.P., Hackett, J.E., Burdges, K.P., and Lyman, V., "Exploratory Studies of the Cruise Performance of Upper Surface Blown Configurations," NASA CR-3193, July 1980.